Supplementary Information

(1) Implementation details of the finite element scheme.
(2) Parametric study regarding the effect of ice sheet thickness on the closing of crevasses using linear-elastic and viscoplastic rheologies.
(3) Parametric study on the role of ice-sheet temperatures on stagnating crevasse propagation due to freezing.
(4) Figure showing the uplift over time using a linear elastic rheology (the linear elastic counterpart of Fig. 10).
(5) Animations showing the deformations and pressure over time for Fig. 6.

Finite element implementation

As described in the main article, the ice-sheet is described by the momentum balance of the ice and rock layers on Ω:

$$\rho_\pi \ddot{\mathbf{u}} - \boldsymbol{L}^T \boldsymbol{\sigma} = \mathbf{0}, \tag{S1}$$

and the fluid contained within the crevasse is described through the mass balance on Γ_d:

$$\frac{\partial q}{\partial \xi} + \dot{h} - \frac{\rho_\mathrm{i}}{\rho_\mathrm{w}} \dot{h}_\mathrm{melt} + \frac{h}{K_\mathrm{w}} \dot{p} = 0 \tag{S2}$$

These two equations are discretised using the finite element method, using quadratic elements for the displacements $\mathbf{u}$, and using quadratic interface elements (Schellekens and de Borst, 1993; Segura and Carol, 2004) for the fluid pressure p. Using the shape functions $\boldsymbol{N}_\mathrm{s}$ for the displacement and $\mathbf{N}_\mathrm{f}$ for the fluid pressure, the state is expressed as a combination of elements or interface elements:

$$\mathbf{u} = \sum_{el} \boldsymbol{N}_\mathrm{s}^{el} \mathbf{u}^{el} \qquad\qquad p = \sum_{iel} \mathbf{N}_\mathrm{f}^{iel} \mathbf{p}^{iel} \tag{S3}$$

using el to indicate the interior elements, and iel for the interface elements. The temporal discretisation is performed using a Newmark scheme for the solid acceleration:

$$\dot{\mathbf{u}}^{t+\Delta t} = \frac{\gamma}{\beta \Delta t} \left(\mathbf{u}^{t+\Delta t} - \mathbf{u}^t \right) - \left(\frac{\gamma}{\beta} - 1 \right) \dot{\mathbf{u}}^t - \left(\frac{\Delta t \gamma}{2\beta} - \Delta t \right) \ddot{\mathbf{u}}^t \tag{S4}$$

$$\ddot{\mathbf{u}}^{t+\Delta t} = \frac{1}{\beta \Delta t^2} \left(\mathbf{u}^{t+\Delta t} - \mathbf{u}^t \right) - \frac{1}{\beta \Delta t} \dot{\mathbf{u}}^t - \left(\frac{1}{2\beta} - 1 \right) \ddot{\mathbf{u}}^t \tag{S5}$$

and an implicit Euler scheme for all time dependent rate terms with the exception of the viscous strain rate:

$$\dot{p}^{t+\Delta t} = \frac{1}{\alpha \Delta t} \left(p^{t+\Delta t} - p^t \right) + \left(1 - \frac{1}{\alpha} \right) \dot{p}^t \tag{S6}$$

$$\dot{h}_\mathrm{melt}^{t+\Delta t} = \frac{1}{\alpha \Delta t} \left(h_\mathrm{melt}^{t+\Delta t} - h_\mathrm{melt}^t \right) + \left(1 - \frac{1}{\alpha} \right) \dot{h}_\mathrm{melt}^t \tag{S7}$$

using time discretisation parameters $\alpha = 1$, $\beta = 0.4$, $\gamma = 0.75$, which results in an unconditionally stable time discretisation. It is assumed that the viscous strain changes slowly compared to all other variables within the system. While it is possible to include the strain increments in a time-implicit manner, we elect here to evaluate this term using an explicit Euler scheme and thus solely require updating this quantity once at the onset of each time increment.

Resulting from this discretisation, the discretised weak form of the momentum balance, Eq. (S1), becomes:

$$\begin{aligned} \mathbf{f}_\mathrm{u} = &\int_\Omega \rho_\pi \boldsymbol{N}_\mathrm{s}^T \boldsymbol{N}_\mathrm{s} \ddot{\mathbf{u}}^{t+\Delta t} + \boldsymbol{B}^T \boldsymbol{D}_\pi \boldsymbol{B} \mathbf{u}^{t+\Delta t} - \boldsymbol{B}^T \boldsymbol{D} \boldsymbol{\varepsilon}_\mathrm{v}^t \, \mathrm{d}\Omega \\ &+ \int_{\Gamma_\mathrm{d}} \boldsymbol{N}_\mathrm{d}^T \boldsymbol{R}^T \mathbf{n} \left(\mathbf{N}_\mathrm{f} \mathbf{p}^{t+\Delta t} - f_\mathrm{t} \exp\left(-\frac{f_\mathrm{t}}{G_\mathrm{c}} \mathbf{n}^T \boldsymbol{N}_\mathrm{d} \mathbf{u}^{t+\Delta t} \right) \right) \, \mathrm{d}\Gamma_\mathrm{d} - \int_\Gamma \boldsymbol{N}_\mathrm{s}^T \boldsymbol{\tau}_\mathrm{ext} \, \mathrm{d}\Gamma = \mathbf{0} \end{aligned} \tag{S8}$$

using the external tractions imposed as boundary condition $\boldsymbol{\tau}_\mathrm{ext}$, the displacement to strain mapping matrix $\boldsymbol{B} = \boldsymbol{L}\boldsymbol{N}_\mathrm{s}$, and the jump operator $[\![\mathbf{u}]\!] = \boldsymbol{N}_\mathrm{d}\mathbf{u}$. The viscous strains within each integration point are updated at the start of each time increment based on Glen's law (Glen, 1955) through:

$$\boldsymbol{\varepsilon}_{\mathrm{v}ip}^t = \boldsymbol{\varepsilon}_{\mathrm{v}ip}^{t-\Delta t} + A_\pi \Delta t \left(\left(\mathbf{u}^{t^T} \boldsymbol{B}^T - \boldsymbol{\varepsilon}_{\mathrm{v}ip}^{t^T} \right) \boldsymbol{D}_\pi^T \boldsymbol{P}^T \boldsymbol{P} \boldsymbol{D} \left(\boldsymbol{B} \mathbf{u}^t - \boldsymbol{\varepsilon}_{\mathrm{v}ip}^t \right) \right)^{\frac{n-1}{2}} \boldsymbol{P} \boldsymbol{D}_\pi \left(\boldsymbol{B} \mathbf{u}^t - \boldsymbol{\varepsilon}_{\mathrm{v}ip}^t \right) \tag{S9}$$

This nonlinear equation is solved using a standard return-mapping scheme. As the strains depend on the displacements of the previous time increment due to the chosen discretisation scheme, this only needs to be performed once per time increment. This has the added advantage that the momentum balance, Eq. (S8), is linear throughout the domain Ω, and thus the contribution of this domain to the total tangent matrix only has to be calculated once per time increment, greatly increasing the computational

efficiency. It should be noted that the interface-related terms of Eq. (S8) are still non-linear, and thus the tangent matrix contributions arising from this term are re-calculated each increment.

The mass balance for the fluid, Eq. (S2), is given in discretised form as:

$$\mathbf{f}_{\mathrm{p}} = \int_{\Gamma_{\mathrm{d}}} \left(\nabla \mathbf{N}_{\mathrm{f}}\right)^T q_{ip}^{t+\Delta t} - \frac{h_{ip}^{t+\Delta t}}{K_{\mathrm{w}}} \mathbf{N}_{\mathrm{f}}^T \mathbf{N}_{\mathrm{f}} \dot{\mathbf{p}}^{t+\Delta t} - \left(1 - \frac{\rho_{\mathrm{i}}}{\rho_{\mathrm{w}}}\right) \mathbf{N}_{\mathrm{f}}^T \frac{{h_{\mathrm{melt}}}_{ip}^{t+\Delta t} - h_{\mathrm{melt}}^t}{\Delta t} - \mathbf{N}_{\mathrm{f}}^T \boldsymbol{N}_{\mathrm{d}} \dot{\mathbf{u}}^{t+\Delta t} \, \mathrm{d}\Gamma_{\mathrm{d}}$$
$$+ \int_{\partial\Gamma_{\mathrm{d}}} k_{\mathrm{p}} \mathbf{N}_{\mathrm{f}}^T \left(p_{\mathrm{ext}} - \mathbf{N}_{\mathrm{f}} \mathbf{p}^{t+\Delta t}\right) \, \mathrm{d}\partial\Gamma_{\mathrm{d}} \tag{S10}$$

where the integration-point level variables h_{melt}, h, and q are obtained by solving a coupled system of equations at each integration point. This two-scale approach is similar to return-mapping schemes, often employed for plasticity modeling (Cormeau, 1975; Sloan, 1987; de Borst and Heeres, 2002). These local variables are described by:

$$q = -2\rho_{\mathrm{w}}^{-\frac{1}{2}} k_{\mathrm{wall}}^{-\frac{1}{6}} f_0^{-\frac{1}{2}} h^{\frac{5}{3}} \left| \frac{\partial p}{\partial \xi} - \rho_{\mathrm{w}} \mathbf{g} \cdot \mathbf{s} \right|^{-\frac{1}{2}} \left(\frac{\partial p}{\partial \xi} - \rho_{\mathrm{w}} \mathbf{g} \cdot \mathbf{s} \right) \tag{S11}$$

$$0 = \rho_{\mathrm{i}} \mathcal{L} \dot{h}_{\mathrm{melt}} + \frac{k^{\frac{1}{2}} T_{\infty} \rho_{\mathrm{i}}^{\frac{1}{2}} c_{\mathrm{p}}^{\frac{1}{2}}}{\pi^{\frac{1}{2}} \left(t - t_0\right)^{\frac{3}{2}}} + q \left(\frac{\partial p}{\partial \xi} - \rho_{\mathrm{w}} \mathbf{g} \cdot \mathbf{s} \right) \tag{S12}$$

$$h = h_{\mathrm{melt}} + \mathbf{n} \cdot [\![\mathbf{u}]\!] \tag{S13}$$

This set of integration-point level equations is resolved in a monolithic manner, first defining the local system of equations given by Eqs. (S11) to (S13) in discretised form as:

$$f_{1,ip} = 0 = q_{ip}^{t+\Delta t} + 2\rho_{\mathrm{w}}^{-\frac{1}{2}} k_{\mathrm{wall}}^{-\frac{1}{6}} f_0^{-\frac{1}{2}} h_{ip}^{t+\Delta t\,\frac{5}{3}} \left| \boldsymbol{\nabla} \mathbf{N}_{\mathrm{f}} \mathbf{p}^{t+\Delta t} - \rho_{\mathrm{w}} \mathbf{g} \cdot \mathbf{s} \right|^{-\frac{1}{2}} \left(\boldsymbol{\nabla} \mathbf{N}_{\mathrm{f}} \mathbf{p}^{t+\Delta t} - \rho_{\mathrm{w}} \mathbf{g} \cdot \mathbf{s} \right) \tag{S14a}$$

$$f_{2,ip} = 0 = \frac{\rho_{\mathrm{i}} \mathcal{L}}{\Delta t} \left({h_{\mathrm{melt}}}_{ip}^{t+\Delta t} - {h_{\mathrm{melt}}}_{ip}^{t} \right) + q_{ip}^{t+\Delta t} \left(\boldsymbol{\nabla} \mathbf{N}_{\mathrm{f}} \mathbf{p}^{t+\Delta t} - \rho_{\mathrm{w}} \mathbf{g} \cdot \mathbf{s} \right) + \frac{k^{\frac{1}{2}} T_{\infty} \rho_{\mathrm{i}}^{\frac{1}{2}} c_{\mathrm{p}}^{\frac{1}{2}}}{\pi^{\frac{1}{2}} \left(t + \Delta t - t_{0\,ip} \right)^{\frac{3}{2}}} \tag{S14b}$$

$$f_{3,ip} = 0 = h_{ip}^{t+\Delta t} - {h_{\mathrm{melt}}}_{ip}^{t+\Delta t} - \mathbf{n}^T \boldsymbol{N}_{\mathrm{d}} \mathbf{u}^{t+\Delta t} \tag{S14c}$$

The above equations define the fluid flux at the integration point through Eq. (S11), the thermal balance through Eq. (S12), and the total opening height through Eq. (S13). This set of equations is solved in a monolithic manner using an iterative Newton-Raphson scheme:

$$\boldsymbol{C}_{ip} \begin{bmatrix} \mathrm{d}q_{ip}^{t+\Delta t} \\ \mathrm{d}{h_{\mathrm{melt}}}_{ip}^{t+\Delta t} \\ \mathrm{d}h_{ip}^{t+\Delta t} \end{bmatrix}_{i+1} = - \begin{bmatrix} f_{1,ip} \\ f_{2,ip} \\ f_{3,ip} \end{bmatrix}_{i}, \tag{S15}$$

where the integration-point level tangent matrix given by Eq. (S16).

$$\boldsymbol{C}_{ip} = \begin{bmatrix} 1 & 0 & \frac{10}{3} \rho_{\mathrm{w}}^{-\frac{1}{2}} k_{\mathrm{wall}}^{-\frac{1}{6}} f_0^{-\frac{1}{2}} h_{ip}^{t+\Delta t\,\frac{2}{3}} \left| \boldsymbol{\nabla} \mathbf{N}_{\mathrm{f}} \mathbf{p}^{t+\Delta t} - \rho_{\mathrm{w}} \mathbf{g} \cdot \mathbf{s} \right|^{-\frac{1}{2}} \left(\boldsymbol{\nabla} \mathbf{N}_{\mathrm{f}} \mathbf{p}^{t+\Delta t} - \rho_{\mathrm{w}} \mathbf{g} \cdot \mathbf{s} \right) \\ \boldsymbol{\nabla} \mathbf{N}_{f} \mathbf{p}^{t+\Delta t} - \rho_{\mathrm{w}} \mathbf{g} \cdot \mathbf{s} & \frac{\rho_{\mathrm{i}} \mathcal{L}}{\Delta t} & 0 \\ 0 & -1 & 1 \end{bmatrix} \tag{S16}$$

$$\begin{bmatrix} \frac{\partial q}{\partial \mathbf{p}} & \frac{\partial q}{\partial \mathbf{u}} \\ \frac{\partial h_{\mathrm{melt}}}{\partial \mathbf{p}} & \frac{\partial h_{\mathrm{melt}}}{\partial \mathbf{u}} \\ \frac{\partial h}{\partial \mathbf{p}} & \frac{\partial h}{\partial \mathbf{u}} \end{bmatrix} = -\boldsymbol{C}_{ip}^{-1} \begin{bmatrix} \rho_{\mathrm{w}}^{-\frac{1}{2}} k_{\mathrm{wall}}^{-\frac{1}{6}} f_0^{-\frac{1}{2}} h_{ip}^{t+\Delta t\,\frac{5}{3}} \left| \boldsymbol{\nabla} \mathbf{N}_{\mathrm{f}} \mathbf{p}^{t+\Delta t} - \rho_{\mathrm{w}} \mathbf{g} \cdot \mathbf{s} \right|^{-\frac{1}{2}} \boldsymbol{\nabla} \mathbf{N}_{\mathrm{f}} & 0 \\ q_{ip}^{t+\Delta t} \boldsymbol{\nabla} \mathbf{N}_{\mathrm{f}} & 0 \\ 0 & -\boldsymbol{N}_{\mathrm{d}} \end{bmatrix} \tag{S17}$$

This system is solved until a converged solution is achieved for the fluid flux, melting height, and total opening height. The tangent is also used to construct a consistent stiffness matrix for the domain-wide equations, defining the derivatives of the integration-point level parameters with regards to the degrees of freedom, as given by Eq. (S17). By using these derivatives within the construction of the global tangent matrix, the stability and convergence rate of the nonlinear solver is greatly

enhanced. The “macro-scale" governing equations, Eqs. (S8) and (S10), are solved in a monolithic manner, solving the system as:

$$\begin{bmatrix} \boldsymbol{K}_{\mathrm{uu}} & \boldsymbol{K}_{\mathrm{up}} \\ \boldsymbol{K}_{\mathrm{pu}} & \boldsymbol{K}_{\mathrm{pp}} \end{bmatrix}_i \begin{bmatrix} \mathbf{u}^{t+\Delta t} \\ \mathbf{p}^{t+\Delta t} \end{bmatrix}_{i+1} = - \begin{bmatrix} \mathbf{f}_{\mathrm{u}} \\ \mathbf{f}_{\mathrm{p}} \end{bmatrix}_i \tag{S18}$$

with the sub-matrices given by:

$$\boldsymbol{K}_{\mathrm{uu}} = \int_{\Omega} \frac{\rho_\pi}{\beta \Delta t^2} \boldsymbol{N}_{\mathrm{u}}^T \boldsymbol{N}_{\mathrm{u}} + \boldsymbol{B}^T \boldsymbol{D} \boldsymbol{B} \, \mathrm{d}\Omega - \int_{\Gamma_{\mathrm{d}}} \frac{f_{\mathrm{t}}^2}{G_{\mathrm{c}}} \exp\left(\mathbf{n} \boldsymbol{N}_{\mathrm{d}} \mathbf{u}^{t+\Delta t}\right) \boldsymbol{N}_{\mathrm{d}}^T \boldsymbol{R}^T \mathbf{n}\mathbf{n}^T \boldsymbol{N}_{\mathrm{d}} \, \mathrm{d}\Gamma_{\mathrm{d}} \tag{S19}$$

$$\boldsymbol{K}_{\mathrm{up}} = \int_{\Gamma_{\mathrm{d}}} \boldsymbol{N}_{\mathrm{d}}^T \boldsymbol{R}^T \mathbf{n} \mathbf{N}_{\mathrm{f}} \, \mathrm{d}\Gamma_{\mathrm{d}} \tag{S20}$$

$$\boldsymbol{K}_{\mathrm{pu}} = \int_{\Gamma_{\mathrm{d}}} \left(\boldsymbol{\nabla} \mathbf{N}_{\mathrm{f}}\right)^T \frac{\partial q}{\partial \mathbf{u}} - \frac{\mathbf{N}_{\mathrm{f}} \mathbf{p}^{t+\Delta t}}{K_w} \mathbf{N}_{\mathrm{f}}^T \frac{\partial h}{\partial \mathbf{u}} - \left(1 - \frac{\rho_{\mathrm{i}}}{\rho_{\mathrm{w}}}\right) \frac{1}{\Delta t} \mathbf{N}_{\mathrm{f}}^T \frac{\partial h_{\mathrm{melt}}}{\partial \mathbf{u}} - \frac{\gamma}{\beta \Delta t} \mathbf{N}_f^T \boldsymbol{N}_{\mathrm{d}} \, \mathrm{d}\Gamma_{\mathrm{d}} \tag{S21}$$

$$\boldsymbol{K}_{\mathrm{pp}} = \int_{\Gamma_{\mathrm{d}}} \left(\boldsymbol{\nabla} \mathbf{N}_{\mathrm{f}}\right)^T \frac{\partial q}{\partial \mathbf{p}} + \frac{1}{K_w} \mathbf{N}_{\mathrm{f}}^T \left(\frac{h}{\Delta t} \mathbf{N}_f - \mathbf{N}_{\mathrm{f}} \mathbf{p}^{t+\Delta t} \frac{\partial h}{\partial \mathbf{p}} \right) - \left(1 - \frac{\rho_{\mathrm{i}}}{\rho_{\mathrm{w}}}\right) \frac{1}{\Delta t} \mathbf{N}_{\mathrm{f}}^T \frac{\partial h_{\mathrm{melt}}}{\partial \mathbf{p}} \, \mathrm{d}\Gamma_{\mathrm{d}} \tag{S22}$$

using the partial derivatives from Eq. (S17). These tangent matrices, with the exception of the constant part of the $\boldsymbol{K}_{\mathrm{uu}}$ sub-matrix, are updated after each iteration based on the updated displacements and pressures, resulting in an optimal convergence rate.

This monolithic solver uses an energy-based convergence criterion $[\mathbf{f}_{\mathrm{u}}\ \mathbf{f}_{\mathrm{p}}][\mathrm{d}\mathbf{u}\ \mathrm{d}\mathbf{p}]^T < \epsilon$, placing equal importance on the convergence of the nonlinear CZM and the fluid pressure within the crack. Once the solution is converged, the stresses ahead of the crack along a pre-determined path are calculated. The stresses are compared to the tensile strength to determine fracture propagation. If the crack propagates, a single new interface element is inserted and more iterations of the monolithic solver are performed (including checking for additional fracture propagation) to obtain a solution in which both the state variables and the fracture location are implicit in time.

References

Cormeau, I.: Numerical stability in quasi-static elasto/visco-plasticity, International Journal for Numerical Methods in Engineering, 9, 109–127, https://doi.org/10.1002/nme.1620090110, 1975.

de Borst, R. and Heeres, O. M.: A unified approach to the implicit integration of standard, non-standard and viscous plasticity models, International Journal for Numerical and Analytical Methods in Geomechanics, 26, 1059–1070, https://doi.org/10.1002/nag.234, 2002.

Glen, J. W.: The creep of polycrystalline ice, Proceedings of the Royal Society of London. Series A. Mathematical and Physical Sciences, 228, 519–538, https://doi.org/10.1098/rspa.1955.0066, 1955.

Schellekens, J. C. J. and de Borst, R.: On the numerical integration of interface elements, International Journal for Numerical Methods in Engineering, 36, 43–66, https://doi.org/10.1002/nme.1620360104, 1993.

Segura, J. M. and Carol, I.: On zero-thickness interface elements for diffusion problems, International Journal for Numerical and Analytical Methods in Geomechanics, 28, 947–962, https://doi.org/10.1002/nag.358, 2004.

Sloan, S. W.: Substepping schemes for the numerical integration of elastoplastic stress-strain relations, International Journal for Numerical Methods in Engineering, 24, 893–911, https://doi.org/10.1002/nme.1620240505, 1987.

Parametric studies of the role of viscous creep for variable thicknesses.

To show our findings related to the role of viscous deformations are valid not just for a single case, but are more generalisable, simulations are performed using an ice sheet thickness ranging from $100\ \mathrm{m}$ to $500\ \mathrm{m}$. The temperature throughout the ice sheet is set to $0\ ^{\circ}\mathrm{C}$, avoiding the need of either scaling the temperature profile used within the main article, or obtaining representative profiles for all thicknesses. Elements with a characteristic size of $5\ \mathrm{m}$ are used near the crevasse, whereas larger element are used within the ice sheet. All other properties correspond to those reported in Table 1.

Fig. S1a shows the development of the downward crevasse and sideways cracks over time. For both the linear-elastic and viscoplastic models, the water pressure at the base of the $100\ \mathrm{m}$ thick ice sheet is not sufficient to cause sideways cracks to develop, as the stresses induced by the hydrostatic fluid pressure do not exceed the weight of the ice and tensile strength. Starting from the $200\ \mathrm{m}$ ice sheet heights, sideways cracks do develop. For the linear-elastic rheology, the sideways propagation rate decreases for the $300\ \mathrm{m}$ case, and fully stops for the $400\ \mathrm{m}$ and $500\ \mathrm{m}$ cases. The mechanism that stops the sideways cracks from developing is the same as observed for the $980\ \mathrm{m}$ case from the main paper: The bending of the ice sheet causes the crack mouth to become restricted and eventually close, preventing fluid from entering the crevasse as shown in Fig. S2a. It should be noted that due to the larger element size used compared to our main results, these fluid fluxes show oscillations due to the element size in the linear-elastic case. In contrast, the fluid inflow is never halted for the viscoplastic simulations for any ice sheet heights except the $100\ \mathrm{m}$ thickness (Fig. S2b). Instead, episodic crack propagation is observed upon reaching the ice sheet bed, as shown in Fig. S1b, with the sideways cracks having short periods of propagation alternating with pauses where the water inflow is fully balanced by the opening created by viscous deformations. This matches the behaviour observed for the $980\ \mathrm{m}$ thick ice sheet from our main paper.

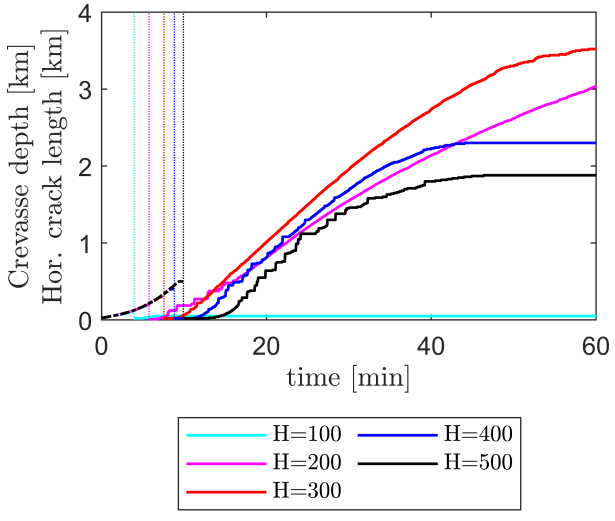

(a) Linear-Elastic

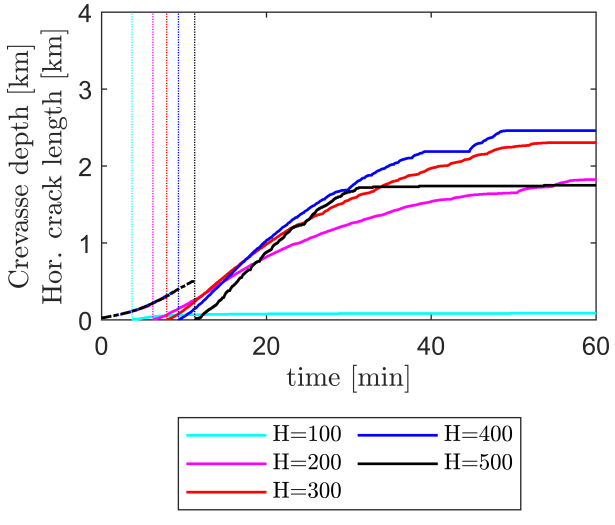

(b) viscoplastic

Figure S1. Crevasse depth (dashed lines) and horizontal crack length (solid lines) for varying ice sheet thickness using a linear-elastic (a) and viscoplastic (b) rheology. Vertical dotted line indicates the moment the vertical crevasse reaches the base of the ice sheet, a which point the horizontal crack propagation begins.

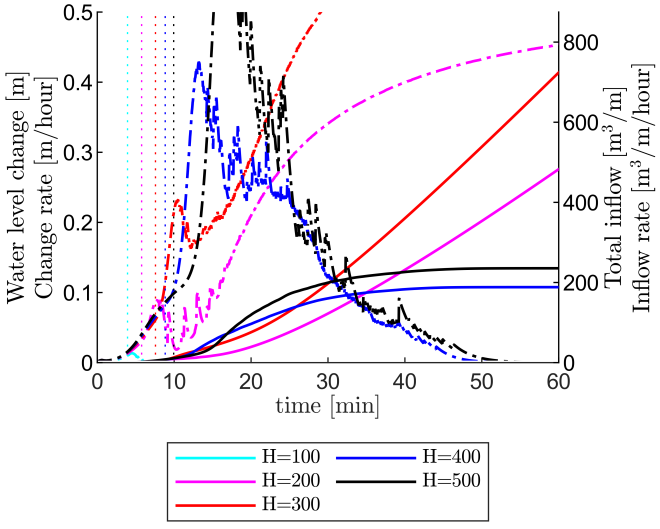

(a) Linear-Elastic

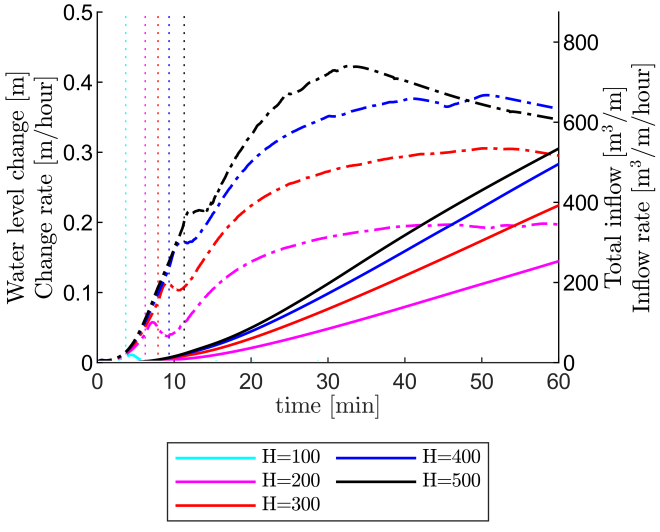

(b) viscoplastic

Figure S2. Lake water level (solid) and rate of water level change (dashed) for varying ice sheet heights using a linear-elastic (a) and viscoplastic (b) rheology. Vertical dotted line indicates the moment the vertical crevasse reaches the base of the ice sheet.

Parametric studies of the role of temperature changes.

Our results do not show a significant role of thermal processes (melting and freezing) on the crevasse and horizontal crack under the depth-dependent temperature profile used in the paper. However, this does not mean such a role does not exist under more "artificial" circumstances. Here, we consider an ice-sheet with a constant temperature, and perform a parametric study on the effect of this temperature for a $300\,\mathrm{m}$ thick ice-sheet. To isolate the role of thermal processes from changes in material parameters with temperature, a constant viscous creep coefficient $A = 5 \cdot 10^{-24}$ and tensile strength $f_\mathrm{t} = 0.3\,\mathrm{MPa}$ are used for all temperatures. Results form these simulations are shown in Fig. S3. More negative temperatures slow the initial crevasse propagation rate, and at temperatures of $-8\,^\circ\mathrm{C}$ halt propagation altogether, as shown in Fig. S3a. This effect, however, is limited to the onset of crevasse propagation, during sideways crack propagation, similar propagation rates are observed, with the sole difference being an offset due to the lower starting rate. For the case in which the crevasse stops altogether, this occurs within the upper $50\,\mathrm{m}$ of the ice-sheet and requires a near-surface temperature of $-8\,^\circ\mathrm{C}$, which due to the proximity of a supraglacial lake required to sustain the hydraulic crevasse propagation is an unrealistic scenario. Similar results are seen in the effect of the crevasse on lake drainage, shown in Fig. S3b: Similar inflow rates that are offset due to lower initial crack propagation.

The thermal energies created due to friction, and conducted away from the fracture due to conduction are shown in Figs. S3c and S3d. It is important to note that these thermal fluxes are provided for the complete surface: As the crevasse stagnates for the $-8\,^\circ\mathrm{C}$ case, less surface area is exposed by the crevasse, and thus less heat is conducted into the surrounding ice. These results indicate that the total heat flux required to stagnate crack propagation initially is fairly small, equivalent to freezing an ice layer with a thickness of $1.5\,\mathrm{mm}$ on average over the $10\,\mathrm{m}$ of newly created crevasse. However, as the crevasse is newly created, viscous creep has not yet had the opportunity to enhance the crevasse opening. As a result, this small amount of freezing suffices to fill the crevasse, and prevent it from pressurising and propagating further.

These results show that the onset of propagation is a critical moment where freezing could prevent the crevasse from forming, whereas the role of conduction, frictional heating, and melting/freezing becomes much less significant for ongoing crevasse propagation, for horizontal cracking, and for the overall ice-sheet uplift and lake drainage process.

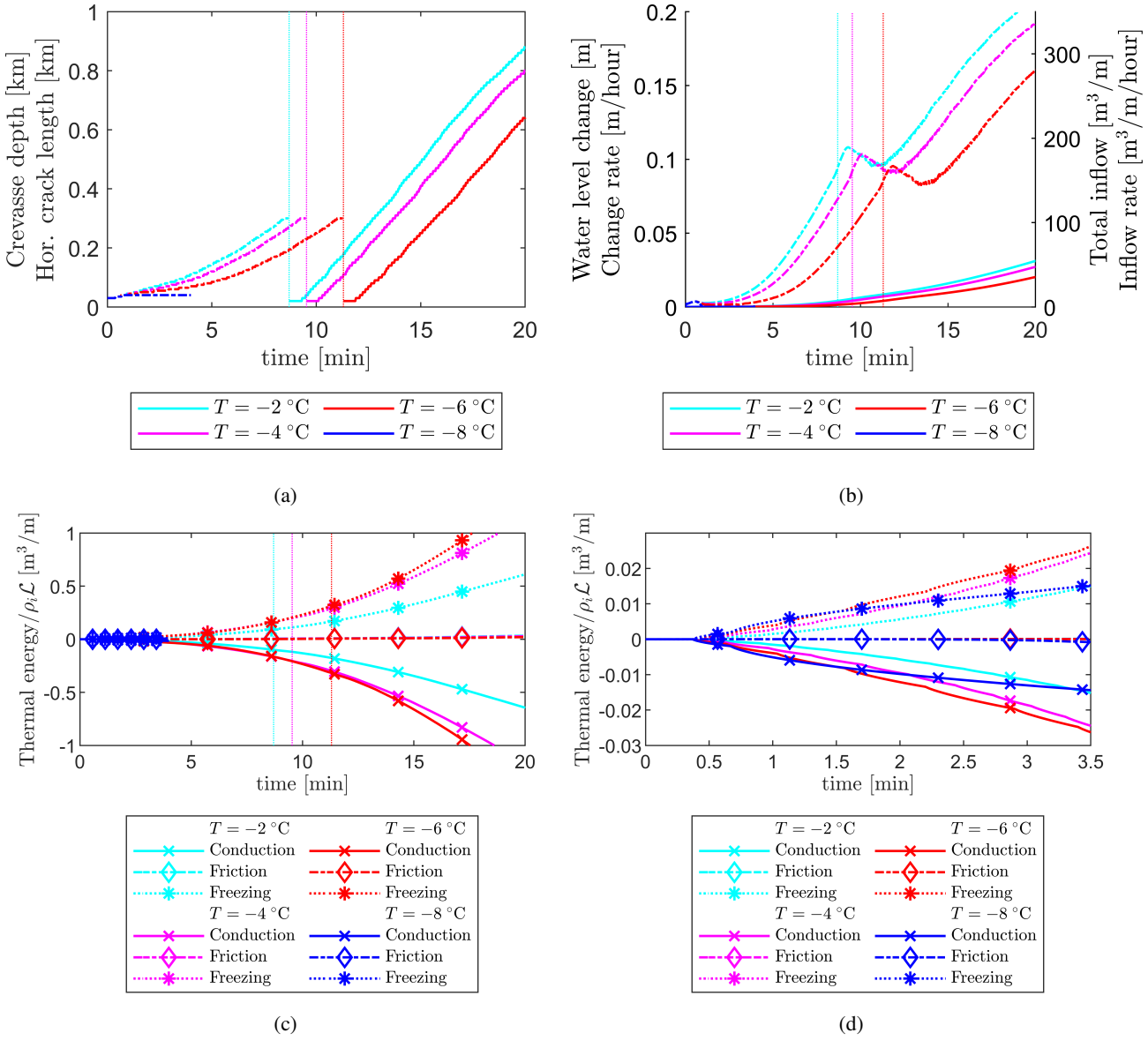

Figure S3. Influence of ice temperature (taken constant throughout the full thickness) on the (a) Crevasse depth and horizontal crack length, (b) Fluid inflow and lake waterlevel changes, and (c&d) thermal energies created and dissipated. $T = -8\,^{\circ}\mathrm{C}$ case only shown up to the point where the crevasse freezes shut.

(Figure) Vertical ice-sheet uplift for a linear-elastic rheology

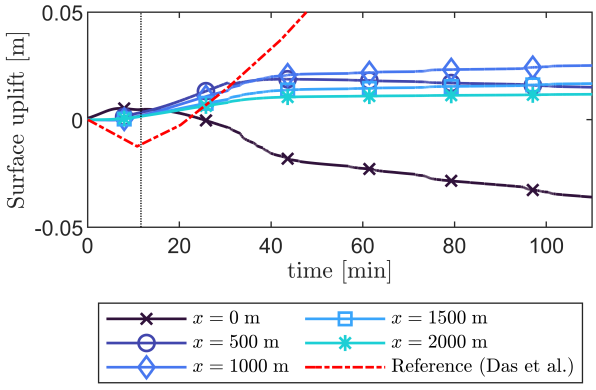

Figure S4. Vertical uplift of the ice sheet surface over time at set distances from the crevasse ($x = 0$ m is at the crevasse, $x = 500$ m is 500 meters to the right of it, etc.), using a linear elastic rheology. Reference results from observations by *Das et al* (Das et al., 2008) are also included. Vertical dotted line indicates the moment the crack reaches the base of the ice sheet. Please note that a shorter vertical scale is used for this linear elastic case, compared to the visco-plastic results from Fig. 6. (0.05 m vs 0.5 m), as much lower uplift (and a stagnation in uplift) are observed.

(Animations)

Animation showing deformations of a linear-elastic ice-sheet and over-pressure relative to the static ice pressure for the cases shown in Figure 2a of the main article. Deformations are scaled by $\times 1000$.
FOR PEER REVIEW ONLY: MOVIE ACCESSIBLE VIA https://www.dropbox.com/scl/fi/14yjvxbjk3hifv9xojkxn/Fig2A_LinearElastic.mp4?rlkey=o7jbavmm8o8d6c2fyumotyj17&dl=1

Animation showing deformations of a visco-plastic ice-sheet and over-pressure relative to the static ice pressure for the cases shown in Figure 2b of the main article. Deformations are scaled by $\times 1000$. A note regarding the ice penetrating the rock layer: The ice-rock contact for the discontinuity is modelled using a penalty approach, scaling the reaction forces with the amount of penetration. As such a penetration of a couple cm occurs to scale this reaction force to a level where it can support the ice-sheet.
FOR PEER REVIEW ONLY: MOVIE ACCESSIBLE VIA https://www.dropbox.com/scl/fi/hbx89n0ivdy68vqxxbviv/Fig2B_ViscoPlastic.mp4?rlkey=2u0839kqn8siqvdd7xd0j5ysa&dl=1